Journal of Metals, Materials and Minerals, 35(2), e2241, 2025

Synergistic effects of Co-Ni nanoalloys on SiO_2@TiO_2: A novel approach to photocatalytic tetracycline degradation

Pratyush Kumar SAHU[1], Alaka RATH[1], Aslisha CHAMPATI[1], Ashish MADUAL[2], Pravat Manjari MISHRA[2], Abanti PRADHAN[1], Brundabana NAIK[1,*]

[1] *Department of Chemistry, ITER, Siksha 'O' Anusandhan, deemed to be University, Bhubaneswar, Odisha, India*
[2] *CSIR-Institute of Materials and Minerals Technology, Bhubaneswar, Odisha, India*

***Corresponding author e-mail**: brundabananaik@soa.ac.in

Received date:
18 December 2024
Revised date:
29 April 2025
Accepted date:
3 May 2025

Keywords:
Photocatalysis;
Visible light;
Core-shell;
Photodegradation;
Synergistic effect

Abstract

To develop a cost-effective alternative to noble metal catalysts for photocatalysis, we synthesized a series of bimetallic Co-Ni nanoalloys on core-shelled SiO_2@TiO_2 nanostructures via a chemical reduction approach. The research demonstrates the photocatalytic behaviour of the Co-Ni alloy-enhanced SiO_2@TiO_2 (ST-Co, Ni) hybrid nanocatalyst, focusing on its crystalline structures, morphological shapes, chemical conditions, and optical properties, utilizing techniques such as X-ray diffraction, field emission scanning electron microscopy, UV-visible diffuse reflectance spectroscopy, photoluminescence spectroscopy, transmission electron microscope, and electrochemical analysis. The catalyst was evaluated for its effectiveness in degrading tetracycline, an overused antibiotic that persists in aquatic environments and is known for negatively impacting water quality. The Co-Ni nanoalloys were tested in various ratios (1:1, 1:2, 2:1), with the 1:1 ratio (ST-Co, $Ni_{1:1}$) emerging as the most effective, achieving a degradation rate of 88.4% at pH 5 in 120 min. This optimal catalyst demonstrated superior charge carrier separation and enhanced absorption of solar radiation in the visible spectrum. Improved solar light absorption and surface plasmon resonance work in concert to promote effective charge transfer from the nanoalloys to the titania, which is probably the cause of the observed photocatalytic degradation rates. So the proposed hybrid nanocatalyst paves the way for photocatalysis and can be suitable for different photocatalytic processes.

1. Introduction

Therapeutic drugs are essential commodities necessary for medical advancement and to raise the standard of living for the growing population. Among various essential pharmaceutical drugs, antibiotics are used enormously. It is often utilized for medication against illness-causing bacteria, growth promoters in the agricultural sector and animal husbandry to facilitate profitability [1]. Penicillin referred to as the wonder drug was the first antibiotic to be discovered by Fleming [2]. The drugs with antibacterial properties namely are sulfonamide, macrolides, fluoroquinone, and tetracycline. Various studies on antibiotic production and consumption suggested that tetracycline (TC) is the most widely used antibiotic drug worldwide due to its global label manufacturing and affordability [3]. Its basic chemical structure is a tetracyclic ring featuring various hydroxyl, methyl, keto, and dimethyl amino groups. It is conventionally employed in various contexts, ranging from livestock farming, agricultural commodities, fish farming, and treating ailments caused by bacteria [4]. It is estimated that it cannot be readily absorbed by either humans or animals, which causes it to seep into surrounding ecosystems and water bodies up to 80% to 90% of its metabolic intermediates are in the form of defecated faeces and urine due to unethical production and consumption [3]. These remnants have detrimental effects on both land and water-dependent organisms due to remaining chemical activity with a substantially high hydrophilic nature and physiological durability. These properties can also be upgraded and passed down via the nutrition cycle which could have a major negative impact.Thus, to safeguard both human health and preserve the ecosystem from these pollutants, it is of utmost necessity to eliminate its harmful undegraded metabolites [5]. As a result, numerous attempts like physical adsorption and advanced oxidation processes (AOPs), have been developed previously for removing antibiotic and microbial contamination because of TC's enormous molecular weight and broad antimicrobial range, but traditional approaches proved inadequate. The most effective method for pollutant degradation is photocatalysis, which uses sophisticated oxidative processes to break down organic pollutants into less toxic components [6]. Its affordability, ease of use, high efficiency, and ease of application make it the most cost-effective method available. Additionally, it supports low energy consumption, less need for extra chemicals, recoverability, and reusability [7]. Photocatalysis generates reactive oxygen species (ROS) through light-induced e^--h^+ pairs, where h^+ oxidizes water or hydroxyl ions to produce hydroxyl radicals ($^{\bullet}OH$) [8,9], while e^- reduce oxygen to form superoxide ($^{\bullet}O_2^-$) [10,11]. These radicals exhibit strong oxidative potentials, enabling applications in pollutant degradation and chemical synthesis, $^{\bullet}OH$ acts as a potent oxidizer and $^{\bullet}O_2^-$ participates in redox

chain reactions. Among different AOPs, a Wide range of semiconductor-based materials including titania (TiO_2), strontium titanate ($SrTiO_3$), cadmium sulfide (CdS), bismuth vanadate ($BiVO_4$), tantalum nitride (Ta_3N_5), tantalu, oxy-nitride (TaON), graphitic carbon nitride (g-C_xN_y), silver phosphate (Ag_3PO_4), and their nano-scale structural units, have been frequently used as photocatalysts for harnessing solar power to perform redox chemical reactions to produce oxidative stress [12-16]. The catalysts are incorporated with various semiconducting materials to increase their photostability and enhance their efficiency. The initial attempts in this direction were developing composites out of multiple components. The materials emerged in contace with one another using artificial means, allowing charge to transfer between the components. However, the incorporation of one part over the other was frequently irregular, and the defects resulting from the contact between the components caused the catalytic performance to be lost. This is mainly because of electron-hole recombination. Forming a core-shell type structure is one of the suitable approaches to get around these shortcomings having multiphasic nanomaterials (MNPs) with an exterior shell composed of several components and an interior core structure [17]. Immobilizing MNPs on solid supports made of mesoporous silica has proven to be one of the most effective methods and may improve their stability and dispersion. Because of their uniform spherical shape and chemical stability, silica nano-spheres are thought to be among the most promising options for MNPs catalytic supports [18]. It has been observed that plasmonic component assembly on the TiO_2 matrix enhances the absorption of radiation up to the visible range [19]. When compared to pure metallic nano-particles, bimetallic nanoparticles whether in alloy or core shell form display distinct electrical, optical, and catalytic properties. Because of their superior electron conductivity and possible uses in lead-free solder alloys, transition metal nanoalloys, like Cu-Ag bimetallics in particular, have attracted signficant interest. The polyol approach has been extensively researched in the last ten years for the systhesis of metal particles, such as copper and silver. Bimetallic alloys such as Ni-Co, Pd-Ag, Pt-Au, Cu-Ag, and Pt-Fe, as well as elemental metals like Ni, Co, Cu, Au, Ag, Pt, Cd, Pd, and Fe, have been successfully created using this method.

Over the past decade, the polyol method has been widely studied for synthesizing metal particles, including copper and silver. This technique has successfully produced elemental metals such as Co, Ni, Cu, Ag, Au, Pt, Pd, Cd, and Fe, as well as bimetallic alloys like Co-Ni, Ag-Pd, Au-Pt, Ag-Cu, and Fe-Pt [20,21]. However, one of the biggest limitations of plasmonic noble metal model catalysts is its costliness such as Pt, Ag and Au. Thus, it is necessary for the development of affordable noble metal-free alternat nanoalloy hybrid catalysts. The established functional features of bimetallic nanoalloy-based catalysts are promising because of their synergistic effects. Cost-effective plasmonic metals such as Ag, Cu, Al, Co, Ni, and Bi can becomebined to create bimetallic nanoalloys that can be used to create hybrid nanocatalysts that have better efficiency across the whole solar band. Recently, Zhu *et al.* [22] synthesized Co-Mn bimetal alloy confined SiO_2 carbon layer core-shell for photodegradation of peroxymonosulfate that reached a maximum degradation value of 95.2%. Lai et al. [23] synthesized Cu@Co plasmonic bimetals by a facile synthesized strategy that showed a photocatalytic CO evolution of 11043.33 $\mu mol \cdot g^{-1}$ with ultra-high CO selectivity (98%). Liang *et al.* [24] synthesized a Ga_2O_3 core-shell structure by chemical modification of Cu/W/Mo/Ni for photo-degradation of methylene blue (92%) and Congo red (79%). Mishra *et al.* [25] developed Bi-Fe mono and bimetals loaded TiO_2 by wet impregnation method, where 1% Bi-TiO_2 showed the highest degradation rates of 80% for methylene blue in two hours. Talreja *et al.* [26] synthesized Fe/Zn-BiOI core-shell that enabled a bandgap of 2.19 eV and the metal loading showed the maximum photodegradation rate of 98% for tetracycline drug at an optimum pH of 10. Also, Bi-based nano-composites have gained far more attention in photocatalysis. Li *et al.* [27] synthesized an in-situ s-scheme $Mn_{0.5}Cd_{0.5}S$/BiOBr oxygen vacancies rich photocatalyst with excellent photo-responsive and internal electric field, which showed exceptional photoreduction of Cr (VI) and photodegradation of tetracycline. Shen *et al.* [28] synthesized a noble s-scheme Ag/$Ag_6Si_2O_7$/$Bi_{12}O_{17}Cl_2$ photocatalyst that reached a rate of 0.0260 min^{-1} for tetracycline degradation, which is largely due to the formation of plasmonic heterojunction in the composite framework providing a robust photocatalytic mechanism. Li *et al.* [29] further synthesized carbon dots and $Mn_{0.5}Cd_{0.5}S$ modified BiOBr s-scheme photocatalyst which showed a destructive 3.1 fold photo-degradation of tetracycline when compared to pristine materials, where carbons dots act as the electron collectors from $Mn_{0.5}Cd_{0.5}S$, which sufficiently enhanced the overall charge separation properties ultimately enhancing the photocatalytic activity. Preeti *et al.* [30] hydrothermally synthesized TiO_2 and loaded Bi/Zn bimetals by wet impregnation method. By loading metal, the material facilitated visible light harvestation and showed the maximum photocatalytic degradation of nitrobenzene (50 ppm) up to 90%. Our team previously reported a cost-effective SiO_2@TiO_2 core-shell structure using a modified Stober process followed by sol-gel-assisted coating, along with Cu-Ag bimetal loading via a facile chemical reduction method [31]. This approach enhanced the visible light absorption properties of the material and showed its physicochemical characteristics. The Ag-Cu (1:3) deposited SiO_2@TiO_2 nano-hybrid demonstrated the highest photocatalytic hydrogen production rate and effective phenol oxidation. Our group previously reported on Au-Cu bimetals loaded on TiO_2@B-g-C_3N_4, where Au-Cu on the dyad interface improves migration, charge separation, and light absorption over a wide range. It produces around three times as much hydrogen (2150) as its mono-metallic equivalents [32]. By altering the surface charge density or by expanding the surface area and pore volume of the TiO_2-base catalyst, its adsorption capability may be easily increased. Additionally, SiO_2 is an excellent support and adsorptive substrate that makes it simple for organic molecules to absorb and transfer to the active sites of TiO_2. Furthermore, SiO_2 and TiO_2 may interact to produce oxygen vacancies that facilitate charge-transfer reactions and, as a result, increase photocatalytic activity. The synthesis of core-shell nano-structures is one way to optimize the SiO_2-TiO_2 interaction. Ikeda *et al.* [33] demonstrated a TiO_2 core@hollow SiO_2 shell nanostructured catalyst to increase the photodecomposition of acetic acid. In a similar way, Ren *et al.* [34] developed a rattle-type TiO_2@void@SiO_2 nano-structure which enhanced the photocatalytic degradation of rhodamine blue dye. The enhanced photoactivity of such nanohybrid is largely due to the empty area between the core and the shell which makes it simple for organic molecules to reach the TiO_2 active sites. A core-shell architecture (TiO_2@SiO_2) offers a better separation rate of the photo-

generated electrons and holes by limiting electron-hole recombination through the close interaction of silica with the titania surface, even though rattle-type TiO_2@void@SiO_2 systems could offer high dye adsorption ability. Therefore, the ability to control the pore structure, surface area, morphology, and catalyst reactivity is an additional benefit of silica-based core-shell nanocomposites [35,36].

To the best of the authors' knowledge, no Co-Ni nanoalloys have been integrated into a TiO_2 core-shell structure. This study presents experimental findings on how incorporating noble metal-free nanoalloys influences the catalytic properties of a wide bandgap SiO_2@TiO_2 core-shell under visible light. Silica was synthesized using a modified Stober synthesis, followed by a thin titania coating via the sol-gel process. The loading of nanoalloys was accomplished via a chemical reduction. The effective incorporation of all the materials was confirmed through various analytical techniques, including X-ray diffraction (XRD), Fourier-transform infrared spectra (FTIR), Scanning electron microscopy (SEM), Energy dispersive X-ray analysis (EDAX), UV-visible diffuse reflectance spectra (UV-DRS), and Photoluminescence Spectra (PL). Photocatalytic breakdown of tetracycline (TC) was assessed by varying catalyst dose, pH, time, and TC concentration. Scavenging tests were conducted to identify active species in the reaction mechanism, and reusability tests.

2. Experimental methodology

2.1 Materials

Tetraethyl orthosilicate (TEOS) was obtained from SRL chemicals, titanium tetra-isopropoxide (TTIP) was obtained from Sigma-Aldrich chemicals, cobalt nitrate ($Co(NO_3)_2$) was obtained from Merck, nickel nitrate ($Ni(NO_3)_2$) was obtained from Merck, sodium hydroxide (NaOH) was obtained from SRL, sodium borohydrate ($NaBH_4$) was obtained from Merck, acetonitrile was obtained from Merck, titanium tetraisopropoxide (TTIP) was obtained from Merck, ethanol (absolute) was obtained from SRL, 25% ammonia was obtained from Merck, aquivion was obtained from Sigma Aldrich, 2-propanol was obtained from Merck, p-benzoquinone was obtained from Merck, citric acid was obtained from Merck, and dimethyl sulfoxide was obtained from Merck. Throughout the reactions, deionized water from a millipore system was used as the solvent. All the chemicals are of analytical grade and have been used without further purification.

2.2 Synthesis of SiO_2@TiO_2 nanospheres

SiO_2 nanospheres were synthesized using a modified Stober synthesis based on previous methods [31]. In a 1000 mL conical flask, 450 mL of ethanol, 80 mL of water and 7.75 mL of ammonia were combined and vigorously stirred for 60 min. Subsequently, 25 mL of tetraethyl orthosilicate (TEOS) was mixed with the above solution and stirred at room temperature overnight. To remove unreacted particles, the colloidal silica was separated by centrifugation at 10,000 rpm and washed several times with ethanol and distilled water, followed by overnight drying at 80°C yielding the desired SiO_2 nanoparticles.

Next, 1 g of SiO_2 nanoparticles were added to a solution mixture comprising a 3:1 (v/v) ethanol and acetonitrile, along with 4 mL of ammonia, designated as solution A. In a separate beaker (solution B), a 3:1 volume ratio of ethanol and acetonitrile was prepared, and 1 mL of titanium tetraisopropoxide (TTIP) was added, stirring continuously until a homogeneous mixture was achieved. Solution B was then added drop by drop to solution A while stirring for approximately 12 h to ensure proper dispersion. Afterwards, centrifugation was employed to isolate the colloidal particles, which were dried at 100°C and calcined at 600°C for 6 h, resulting in the formation of white powder marked as SiO_2@TiO_2 (ST).

2.3 Synthesis of Co-Ni deposited SiO_2@TiO_2

A total of 0.5 g of the prepared ST was homogenized in 200 mL of deionized water for 30 min. Meanwhile, a 2 mM solution of cobalt (II) nitrate (0.0582 g) and nickel (II) nitrate (0.581 g) was prepared in a 50 mL 4:1 ethanol and deionized water solution. After the 30 min dispersion, this solution was combined with the ST in a reagent bottle, and the pH was adjusted to 9 using 1 M NaOH. A 0.1 M (0.189 g in 50 mL) solution of sodium borohydride (NaBH4) was then added drop by drop until the colour changed to dark, and the mixture was refluxed (aged) in a three neck round bottom flask for 2 h under nitrogen atmosphere. The resulting mixture was centrifuged, washed with water and ethanol repeatedly, dried overnight at 80°C, and calcined for 2 h at 400°C. For comparison, ST hybrid catalysts were synthesized with Co-Ni ratios of 1:1, 2:1, and 1:2, and marked as ST-Co, $Ni_{1:1}$, ST-Co, $Ni_{2:1}$, and ST-Co, $Ni_{1:2}$, respectively. The entire reaction process is demonstrated in Scheme 1.

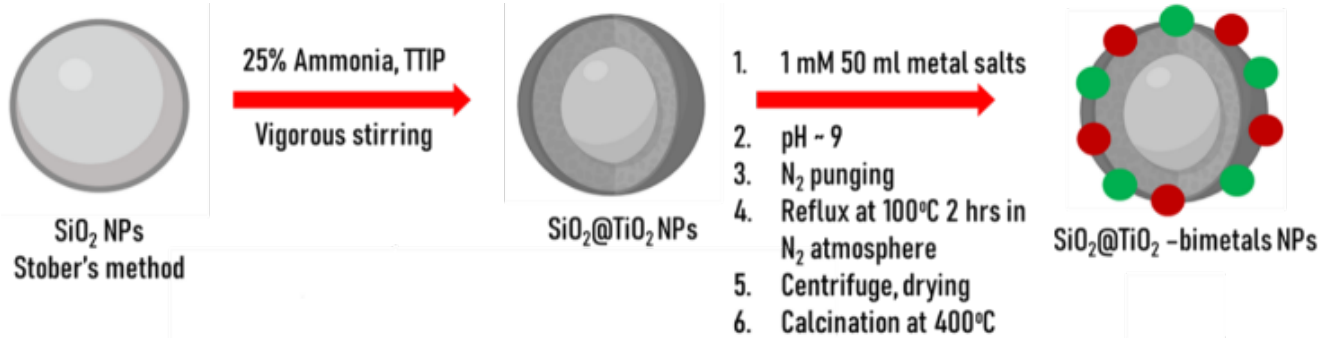

Scheme 1. Synthesis of SiO_2@TiO_2-Co, Ni.

2.5 Electrochemical measurements

A catalyst sample weighing 5 mg was thoroughly mixed with 100 µL of isopropanol, followed by the addition of 5 µL of aquivion binder. This mixture was then homogenized in a sonicator for 10 min to form a slurry, the slurry was then drop-casted onto a 1 cm × 1 cm fluorine doped tin oxide (FTO) electrode. The coated electrode was dried overnight at 60°C, producing a consistent thin film on the FTO surface, which later served as the working electrode for subsequent analyses. Electrochemical measurement was conducted in a conventional three-electrode system, employing a saturated calomel electrode as the reference, platinum wire as the counter electrode, and the FTO film as the working electrode 0.2 M sodium sulfate purged with nitrogen was used as the electrolyte and Mott-Schottky measurements were performed at an applied potential of 0.2 V with a 2 mV AC perturbation signal.

2.6 Sample characterization

Broad-angle X-ray powder diffraction (XRD) patterns of the composites were studied via Bruker AXS D4 using CuKα radiation over a range of 10° to 80°. The molecular vibrations and functional groups were characterized via Perkin Elmer Fourier-transform infrared spectrometer using KBr-based pellets over a range of 400 cm^{-1} to 4000 cm^{-1}. Bandgap studies were obtained via JASCO-750 UV-visible spectrophotometer, which analyzed diffuse reflectance spectra over the range of 200 nm to 800 nm using boric acid reference. Photoluminescence (PL) spectral studies were examined at room temperature with RF-5301 spectrofluororphotometer, SHIMADZU. Surface morphology was examined via Field emission scanning electron microscopy (FE-SEM) and Energy-dispersive X-ray analysis (EDAX) using ZEISS EVO MA 15, Transmission electron microscopy (TEM) was done using JEOL JEM-2100F Electron microscope, and electrochemical studies were done using IVIUM electrochemical work station.

3. Results and discussion

3.1 Sample analysis

The phase identity of the synthesized nanocomposite was thoroughly investigated using XRD analysis, as shown in Figure 1(a). The XRD patterns reveal distinct diffraction peaks that are characteristic of titanium dioxide (TiO_2). Specifically, peaks corresponding to the (101) and (200) planes appear at angles of 25° and 48°, respectively [37]. The strong peak at 25° is particularly significant as it indicates the presence of the anatase phase of TiO_2, which is known for its unique single-layered crystalline structure. Additionally, the analysis provides evidence for the presence of SiO_2 spheres acting as a substrate, as indicated by a peak around 21°. This peak reflects the amorphous nature of silica, further confirming the successful formation of the SiO_2@TiO_2 (ST) core-shell structure. Furthermore, the incorporation of cobalt nanoparticles into the composite introduces additional peaks at the (002) and (004) planes, observed at angles of 5° and 12° respectively [38,39]. This suggests that the cobalt is well-integrated into the nanocomposite. In contrast, nickel nanoparticles contribute a peak at 55°, which is indexed to the (116) plane, providing further confirmation of their presence and alignment within the structure. The small peaks observed correspond to the low loading percentage of metal complexes used in the synthesis, which was kept below 5%. Specifically, only 1 mM of the metal salt was utilized, resulting in a subtle yet detectable signature of the incorporated metal nanoparticles. Overall, the XRD analysis not only elucidates the phase composition and crystallinity of the synthesized nanocomposite but also highlights the successful integration of both SiO_2 and TiO_2, along with the cobalt and nickel nanoparticles, into a cohesive structure [40].

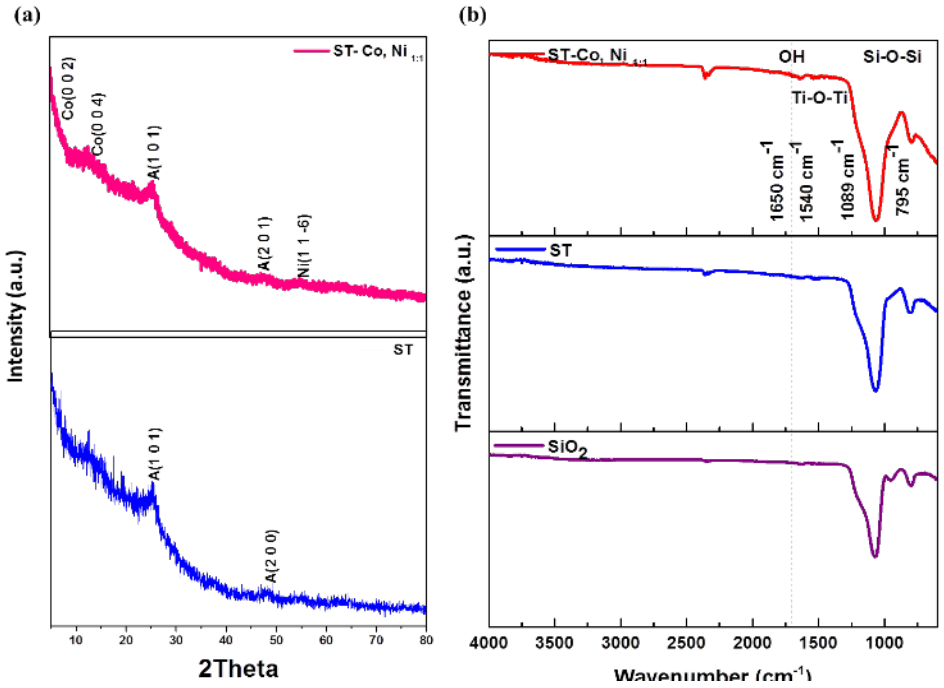

Figure 1. (a) XRD, and (b) FTIR spectra of ST, and ST-Co, $Ni_{1:1}$ nanocomposite.

The FTIR spectra, depicted in Figure 1(b), provide valuable insights into the functional groups present in the synthesized materials. A prominent peak observed around 1100 cm^{-1} indicates the Si-O-Si stretching vibrations, confirming the presence of the silica core within the nanocomposite. This characteristic peak is crucial as it signifies the integrity of the silica framework. In addition to the silica features, the presence of TiO_2 shells is further supported by additional peaks within the range of 500 cm^{-1} to 795 cm^{-1}. These peaks correspond to the stretching vibrations of Ti-O-Ti bonds, which are typical for titanium dioxide structures. This finding aligns with the expected properties of TiO_2 and indicates the successful incorporation of the titanium component into the composite. Moreover, the spectra reveal a peak in the range of 2100 cm^{-1} to 2140 cm^{-1}, which is indicative of C=O stretching vibrations. This particular peak suggests that carbon monoxide (CO) molecules are adsorbed on the surface of the metal nanoparticles, thereby confirming the effective deposition of cobalt and nickel alloy nanoparticles onto the core-shell structure. Overall, the FTIR analysis not only complements the findings from X-ray diffraction (XRD) but also reinforces the hybrid nature of the ST-Co, $Ni_{1:1}$ nanocomposite. The correlation between the FTIR data and XRD results emphasizes the successful synthesis of this composite material, highlighting its potential for various applications [37,39].

To investigate the morphology and shape of nanohybrid that aggregate to form the Co-Ni nano-alloy in ST composite, FE-SEM and TEM analysis was conducted. The images, as shown in Figure 2(a-b) reveal spherical SiO_2 nanoparticles coated with an ultrathin TiO_2 layer. The Co-Ni nano-alloys are uniform across ST surface. As shown in Figure 2(c) EDAX analysis reveals the percentage of all the elements present in the hybrid composite. The distribution of Co-Ni nano-alloy particles is also shown in Figure 2. The uniform dispersion of the Co-Ni alloy with a narrow size distribution on the ST surface is crucial for enhancing catalytic performance [31].

From the UV-Vis DRS spectra, the absorbance was collected to assess the light absorption properties of the photocatalysts. As shown in Figure 3(a), all the photocatalysts demonstrated the ability to absorb visible light, with the absorption maximum increasing upon the incorporation of the Co-Ni alloy. The ST sample exhibited an absorption edge at 290 nm, while there was a shift to 310 nm for ST-Co, $Ni_{1:1}$. This shift indicates enhanced visible light absorption due to Co-Ni loading on TiO_2 [31]. The enhanced absorption for ST-Co, $Ni_{1:1}$ corresponds to the incorporation of Co-Ni bimetals into TiO_2 that introduces new energy levels within its bandgap, facilitating lower-energy electronic transitions and thereby enhancing visible light absorption. This modification leads to a noticeable redshift, further amplified by the synergistic interaction between Co, Ni which optimizes the electronic structure. Additionally, the presence of Co-Ni nanoparticles may induce surface plasmon resonance (SPR), boosting light absorption in the visible region. Their deposition also promotes the formation of defect sites and oxygen vacancies on the TiO_2 surface, which improve charge carrier separation by acting as electron-hole traps, ultimately reducing recombination and enhancing photocatalytic efficiency [31]. The bandgaps of all the nanomaterials were further determined from the Tauc plot (shown in Figure 3(b)). The relationship between absorbance and incident photon energy is as follows:

$$(\alpha h\nu)^{\gamma} = \beta(h\nu - E_g) \quad (1)$$

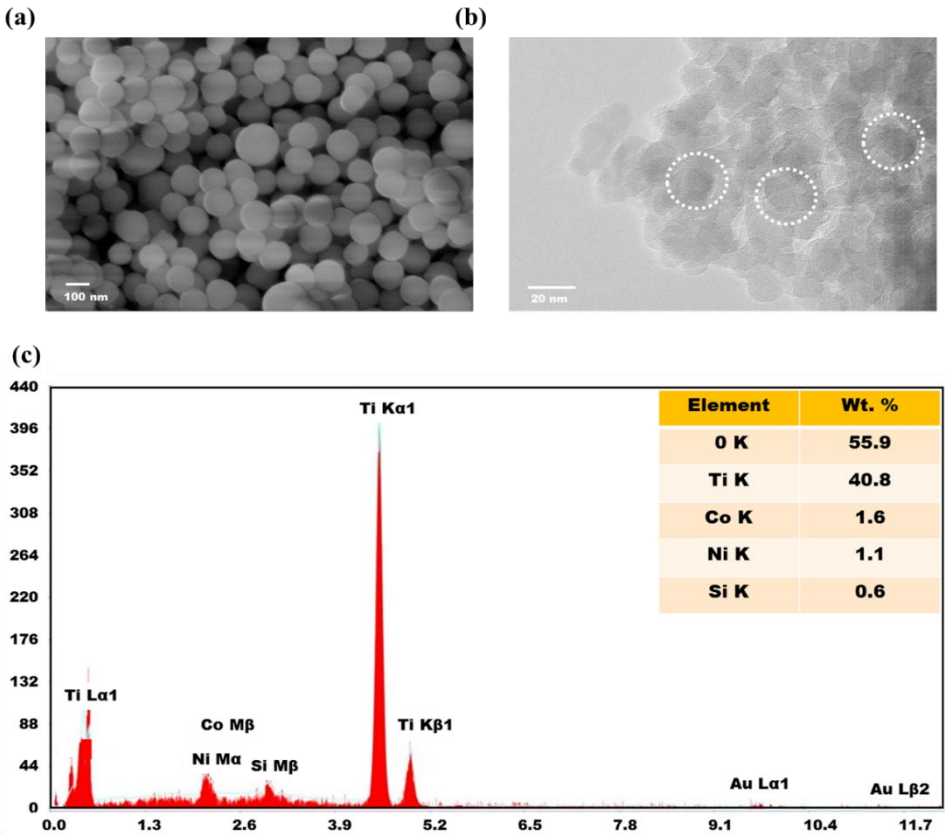

Figure 2. (a), (b) SEM and TEM images for ST-Co, $Ni_{1:1}$ nanocomposite, and (c) EDAX spectra ST-Co, Ni_1

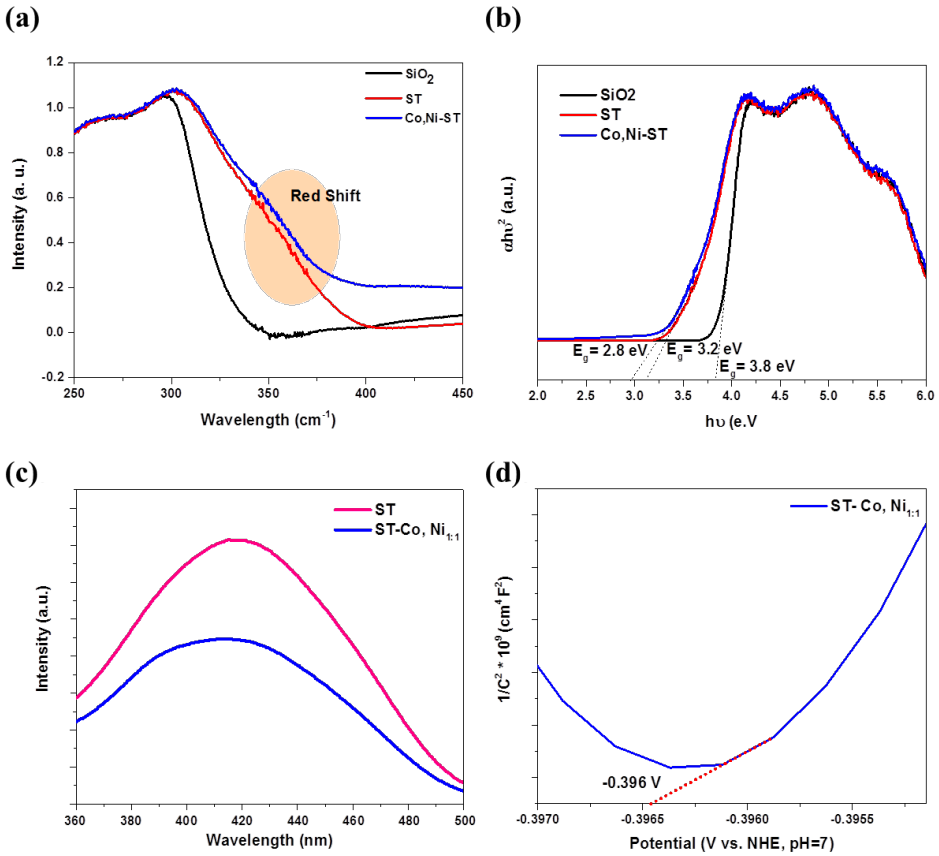

Figure 3. (a) Diffuse reflectance spectra of all composites, (b) Tauc plot for ST-Co, $Ni_{1:1,}$ and (c) PL spectra of ST and ST-Co, $Ni_{1:1,}$ and (d) Mott-Schottky plot of ST-Co, $Ni_{1:1}$.

In a Tauc plot, the relationship between $(\alpha hv)^{\gamma}$ and hv is used to determine the band gap of a material. Here, α represents the absorption coefficient, h is Planck's constant, v denotes the frequency of the incident light, and γ indicates the type of electronic transition. Specifically, when γ = 2, it corresponds to an allowed direct transition, and when γ =1/2, it represents an allowed indirect transition. Additionally, β is the proportionality constant, and E_g refers to the band gap energy, measured in eV [21]. The calculated bandgap values were 3.8 eV for SiO_2, 3.2 eV for TiO_2, and 2.8 eV for ST-Co, $Ni_{1:1}$, respectively [31].

In the equations, E_{CB} and E_{VB} correspond to the CB and VB potentials, respectively, of direct bandgap semiconductors, and E_g refers to the bandgap of the semiconductor in eV, which is determined using the Tauc plot [6]. To investigate the recombination dynamics and charge transfer efficiency of photogenerated electron-hole pairs in semiconductor-based photocatalysts, photoluminescence (PL) spectroscopy was systematically employed. As shown in Figure 3(c), the PL spectra of all synthesized catalysts reveal a dominant emission peak centred at approximately 420 nm, a signature feature linked to radiative recombination processes in TiO_2-based materials. This emission band is widely associated with self-trapped excitons (STEs) formed within distorted TiO_6 octahedral units, where lattice vibrations and structural defects localize charge carriers, promoting non-radiative energy dissipation. The consistency of this peak across samples underscores the structural integrity of the Ti-O framework, which governs excitation behaviour and interfacial charge separation. Notably, reduced PL intensity in bimetals-modified catalysts often correlates with suppressed recombination, as observed in prior studies on defect-engineered TiO_2 [41]. These findings align with the broader understanding that octahedral coordination geometry in transition-metal-oxides critically influences optoelectronic properties, as demonstrated in perovskite and layered titanate systems [42,43]. Hence the charge carrier recombination rate drastically decreases from ST nanocomposite to ST-Co, $Ni_{1:1}$, which can be explained on the basis of transition metal deposition, which enhances charge transportation, and electron mobility in the CB and ultimately enhances photocatalytic activity.

In addition to the determination of bandgap values of the materials the CB band position of the ST-Co, $Ni_{1:1}$ nanocomposite was also determined from the electrochemical measurements. The following equations, as previously reported [6], explain the potentials of the semiconductor valence band (VB) and conduction band (CB), and additional analysis was carried out to investigate the changes in active species throughout the reaction process: where the Mott-Schottky plot (as depicted in Figure 3(d)) shows that the band position was found to be –0.39 V. The VB potential was further determined to be 2.41 V from the equation:

$$E_{CB} = E_{VB} - E_g \quad (2)$$

3.2 Photocatalytic performance against tetracycline degradation

Photocatalytic degradation experiments were carried out using the prepared catalysts, including ST, ST-Co, $Ni_{1:1}$, ST-Co, $Ni_{1:2}$, and

ST-Co, $Ni_{2:1}$ to assess their efficacy in degrading tetracycline (TC) under solar light, as illustrated in Figure 4(a). Prior to the photocatalytic degradation phase lasting 120 min, a 30 min in darkness was employed to establish adsorption-desorption equilibrium between TC and the catalysts. The results indicated an increasing order of photocatalytic degradation efficiency for TC as follows: ST (65.5%) < ST-Co, $Ni_{2:1}$ (77.2%) < ST-Co, $Ni_{1:2}$ (80.3%) < ST-Co, $Ni_{1:1}$ < (83.31%). Special emphasis was placed on the optimization of the ST-Co, $Ni_{1:1}$ catalyst, attributed to the plasmonic effects of bimetals on ST which facilitate the binding and adsorption of substrates on the nanosphere surfaces, leading to enhanced photocatalytic degradation.

The pH of the solution is crucial in optimizing the photocatalytic activity. An investigation into the effect of initial pH levels on the photodegradation efficiency of TC was conducted across a range of pH 3 to pH 9, as depicted in Figure 4(b). The findings revealed that photodegradation efficiency increased with pH, peaking at 5 before declining. pH plays a significant role in photocatalysis by influencing the electrostatic interactions between the semiconductor surface, solvent molecules, substrates, and the charged radicals generated during the reaction. Notably, the highest adsorption efficiency for ST-Co, $Ni_{1:1}$ was recorded at pH 5, highlighting how acidic conditions facilitate better adsorption and improve the photocatalytic degradation of TC. The surface charge of ST-Co, $Ni_{1:1}$ nanocomposites is highly dependent on the pH of the surrounding environment. Typically, TiO_2 exhibits a point of zero charge (PZC) near pH 6.2, while SiO_2 has a much lower PZC, around 2 [44-46]. When the pH of the solution exceeds the PZC, surface hydroxyl groups (Ti-OH and Si-OH) undergo deprotonation, resulting in a negatively charged surface [45,47]. Conversely, at pH values below the PZC, the surface remains positively charged due to protonation. The incorporation of transition metals such as Co and Ni further alters the surface charge of the composite, potentially shifting the PZC and modifying the density of surface acidic groups [45,48]. In our case after loading of Co, Ni bimetals the PZC of the nanocomposites was found out to be 5.4. TC exists in different ionic forms depending on the solution pH, with three main pKa values at approximately 3.3, 7.7, and 9.7. These correspond to the sequential deprotonation of its functional groups, resulting in zwitterionic or negatively charged species as the pH increases [48]. At pH 5, TC predominantly exists as a zwitterion or carries a net negative charge due to the deprotonation of its carboxylic group. At this pH the catalyst surface is slightly positively charged (pH < PZC), which favours the electrostatic attraction of the negatively charged TC species. This interaction enhances the adsorption of the TC onto the catalyst surface, which is a critical step for effective photocatalytic degradation, as it increases the likelihood of the reactive oxygen species (such as $^{\bullet}OH$ and $^{\bullet}O_2^-$) interacting with the pollutant [45,47].

Several operational parameters significantly influence the reaction rate and, consequently, the performance of photocatalysis. Various catalyst amounts, ranging from 0.01 g to 0.06 g, were added to the reaction medium. As shown in Figure 5(a), the results indicated a significant increase in degradation efficiency, reaching a maximum of 88.3% after 120 min with a catalyst dosage of 0.05 g. However, beyond this dosage, the efficiency declined, possibly due to the catalyst's light absorption characteristics. An excessive amount of catalyst may hinder light penetration, thereby restricting the efficacy of photocatalysis.

The photodegradation of TC was studied over a concentration range of 10 ppm to 50 ppm, with the results presented in Figure 5(b). At the optimized concentration of 20 ppm, absorption spectra were recorded at 350 nm at several time intervals: 0, 15, 30, 60, 90, and 120 min. A strong absorption peak at 275 nm was observed initially, but its intensity gradually decreased with time, as shown in Figure 6(a). The highest degradation efficiency was reached at the 120 min mark, a trend consistently observed across all experiments. Additionally, the photocatalytic degradation of TC followed a pseudo-first-order kinetic model. The kinetic analysis presented in Figure 6(b) highlights the relationship between TC concentration and photocatalytic degradation at different time points, confirming a significant correlation with the first-order kinetics equation.

$$K_{app}t = \ln\frac{C_0}{C_t} \quad (3)$$

$$K_{app} = \ln\frac{C_0}{C_t} \times \frac{1}{t} \quad (4)$$

The relationship between Ct (final concentration of TC at any time, t) and Co (initial concentration of TC) is shown in Figure 6 (b), which is expressed as Co/Ct as a function of time for degradation. The rate constant for pseudo-first-order kinetics is indicated by Kapp. In accordance with the first-order kinetics principles, Table 1 illustrates how the Kapp value falls as the solution concentration rises.

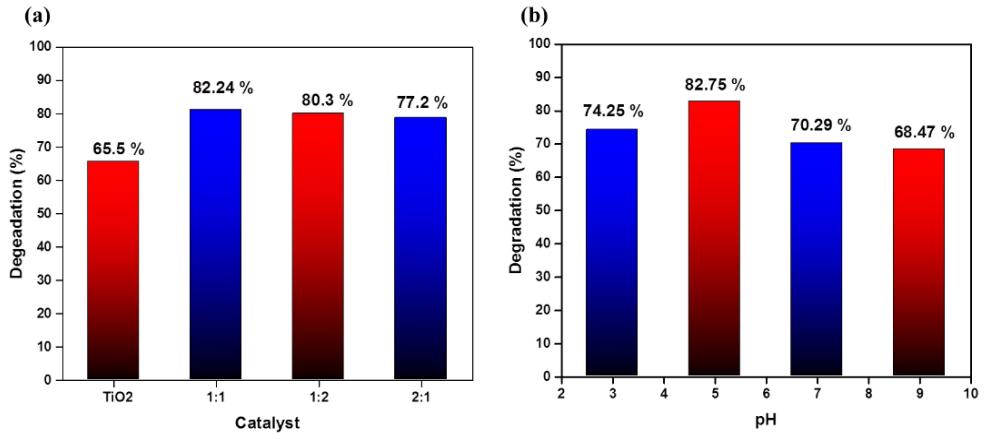

Figure 4. (a) Effect of various catalysts, and (b) Effect of pH on photocatalytic degradation of TC using ST-Co, $Ni_{1:1}$.

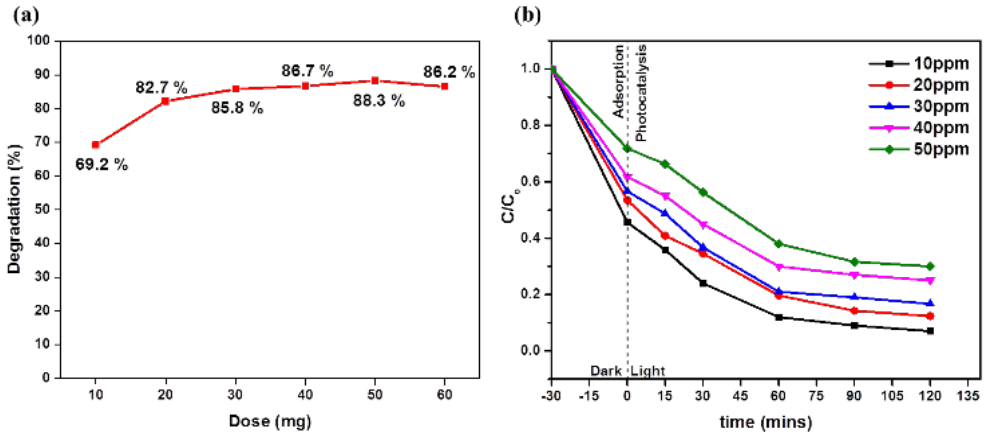

Figure 5. (a) Effect of catalyst doses, and (b) Effect of pollutant concentrations for photodegradation of TC using ST-Co, $Ni_{1:1}$.

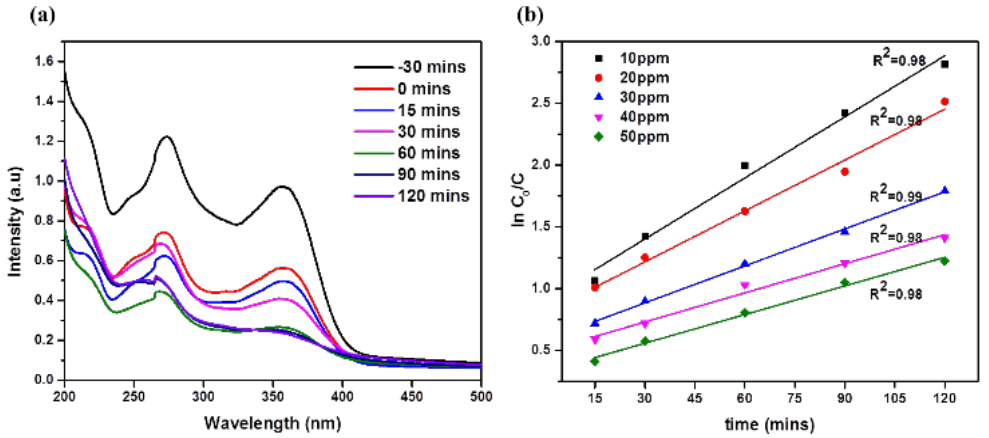

Figure 6. (a) Absorbance peak for photocatalytic degradation of TC at different time intervals, and (b) pseudo-1st order kinetics for different concentration.

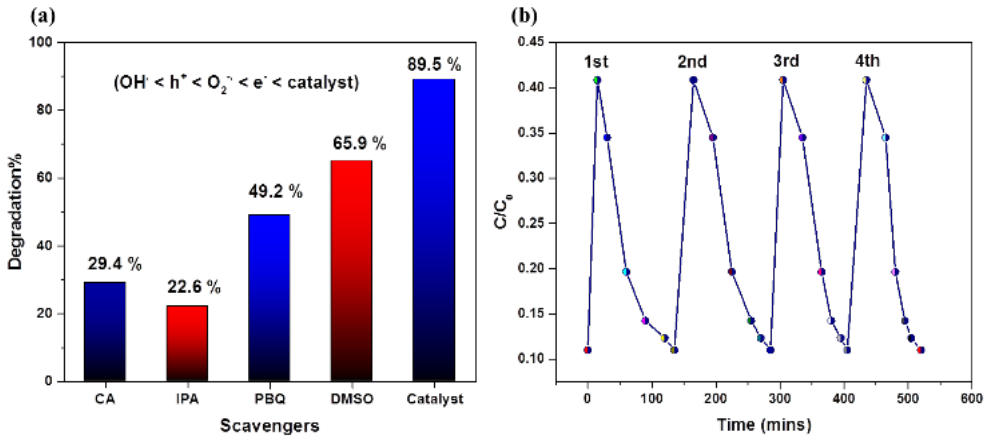

Figure 7. (a) Effect of scavengers on photodegradation of TC, and (b) Catalytic reusability test of ST-Co, $Ni_{1:1}$ towards TC photodegradation.

Table 1. Kinetics study for TC degradation at different concentration values.

Concentration [ppm]	Time [min]	K_{app} [min^{-1}]	Regression coefficient (R^2)
10	120	0.023445	0.98
20	120	0.02096	0.98
30	120	0.014931	0.99
40	120	0.011761	0.98
50	120	0.010201	0.98

The importance of active species in the photodegradation process is frequently underlined. As illustrated in Figure 7(a), a scavenging experiment was conducted with 1:1 as the ideal photocatalyst in order to determine the active species involved in the degradation mechanism of TC. Potential active radicals such as superoxide ($^{\bullet}O_2$), hydroxyl ($^{\bullet}OH$), hole (h^+), and electron (e^-) were captured by a number of scavenging agents, including para-benzoquinone (PBQ), isopropanol (IPA), citric acid (CA), and dimethyl sulfoxide (DMSO). Throughout the experiment, constant reaction conditions and a scavenger concentration of 1 mM were maintained. The inclusion of 76 µL IPA (22.6%) and 0.042 g CA (29.4%) significantly decreased the degradation efficiency, according to the data. Although the addition of 71 µL DMSO (65.9%) and 0.00108 PBQ (49.2%) also lowered the efficiency, the effect was less pronounced. These findings indicate that hydroxyl radicals ($^{\bullet}OH$) and holes (h^+) are the major reactive species responsible for TC degradation, while electrons (e^-) and superoxide ($^{\bullet}O_2$) play a secondary role [49].

From the as-determined bandgap values from the Tauc plot for ST-Co, $Ni_{1:1}$ with 2.8 eV and the Mott-Schottky plot, the CB of ST-Co, $Ni_{1:1}$ (–0.39 eV) is more negative than the $O_2/^{\bullet}O_2^-$ potential (–0.33 eV vs. NHE), allowing O_2 to act as an electron acceptor and be reduced to $^{\bullet}O_2^-$, which can then oxidize tetracycline (TC) into H_2O and CO_2. Additionally, the VB of ST-Co, $Ni_{1:1}$ (2.41 V) is higher than the REDOX potential of $^{\bullet}OH/OH^-$ (+1.99 eV vs. NHE). This means that the photogenerated holes (h^+) can react with adsorbed water molecules to produce hydroxyl radicals ($^{\bullet}OH$). As a powerful oxidant, $^{\bullet}OH$ effectively degrades organic pollutants, ultimately converting TC into CO_2 and H_2O. The addition of Co, Ni bimetals, which have partially filled 3d orbitals, alters the electronic properties of TiO_2 by developing new energy states within its bandgap. These impurity states help narrow the bandgap, enabling better absorption of visible light. On the surface of the catalyst, Co and Ni atoms may form clusters or surface states that act as traps for electrons or assist in charge transfer, enhancing photocatalytic activity. When these ions occupy substitutional or interstitial sites in the TiO_2 lattice, they cause slight distortions that shift energy levels, lowering the energy needed for electron excitation. Furthermore, incorporating Co and Ni improves electrical conductivity and promotes charge separation, contributing to a band-tailing effect that visually reduces the optical bandgap from about 3.2 eV to 2.8 eV. This combined influence of defect states and lattice changes extends light absorption into the visible spectrum, thereby improving the photocatalytic efficiency of TiO_2. The catalyst was also subjected to a recyclability test, where the nanohybrid demonstrated stability over four consecutive cycles (as illustrated in Figure 7(b)). The overall reaction mechanism is illustrated in Figure 8. The particular photodegradation process of TC by the ST-Co, $Ni_{1:1}$ nanohybrid occurs through the following steps:

$$Co,\ Ni\text{-}ST_{1:1} + hv \rightarrow Co,\ Ni\text{-}ST_{1:1}\left(e^- + h^+\right) \quad (5)$$

$$h^+ + OH^- \rightarrow {}^{\bullet}OH \quad (6)$$

$$O_2 + e^- \rightarrow {}^{\bullet}O_2^- \quad (7)$$

$$O_2^{-*} + TC \rightarrow Degradation\ product + CO_2 + H_2O \quad (8)$$

$$^{\bullet}OH + TC \rightarrow Degradation\ product + CO_2 + H_2O \quad (9)$$

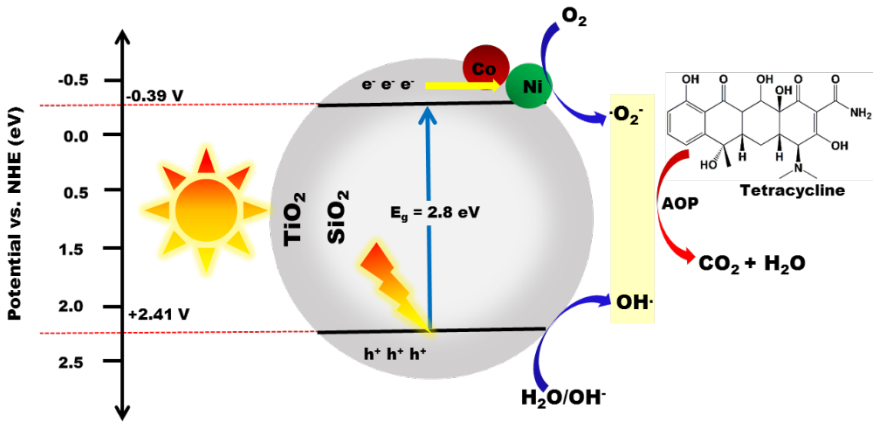

Figure 8. A plausible mechanism for photocatalytic degradation of TC using ST-Co, $Ni_{1:1}$.

The total organic carbon (TOC) analysis was performed to determine the mineralization level of TC under solar light illumination using ST-Co, $Ni_{1:1}$ nanocomposite. As illustrated in Figure 9, the TOC removal trends for TC, using ST-Co, $Ni_{1:1}$ nanocomposite were shown that inclined with solar light exposure till 120 min. For TC, the ST-Co, $Ni_{1:1}$ nanocomposite achieved TOC removal efficiencies of 86.7%. These results indicate that the nanohybrid photocatalyst effectively degrades and mineralizes TC, though some organic carbon remains in the solution. Overall, the data emphasizes that ST-Co, $Ni_{1:1}$ nanohybrid has the potential to improve the degradation rate and mineralization of organic pollutants considerably.

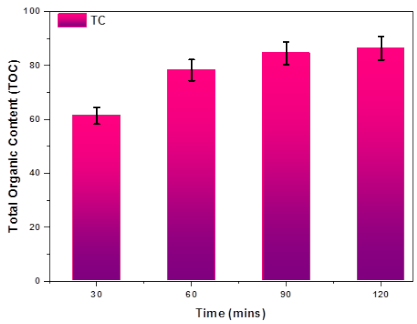

Figure 9. TOC for tetracycline degradation using ST-Co, Ni1:1 nanocomposite.

Recyclability is essential for the economic viability of photocatalysts in environmental and industrial applications. The reusability test of ST-Co, $Ni_{1:1}$ was evaluated through repeated photocatalytic degradation cycles. The catalyst maintained high efficiency over four degradation cycles showing significant stability. Post-use structural analysis indicated strong catalyst durability: XRD patterns (Figure 10(a)) showed minimal peak intensity reduction, indicating slight crystallinity changes without phase transitions. FE-SEM images (Figure 10(b-c) revealed a slight particle size change, supporting the catalyst's structural integrity. These findings confirm that ST-Co, $Ni_{1:1}$ is a reliable and recyclable photocatalyst, suitable for pollutant degradation.

The adopted strategy demonstrates significant potential for improving the photocatalytic efficiency of TiO_2-based materials by extending their light absorption into the visible spectrum while retaining UV activity. Among the various modification approaches-including heterojunction engineering, non-metal doping (e.g., N, S), and metal doping- transition metal doping emerges as a particularly effective method for tailoring TiO_2 band structure and charge carrier dynamics. As evidenced by comparative studies (summarized in Table 2), noble metal surface reactivity. However, balancing cost, stability, and performance remains a critical challenge. Our solution employs core-shell SiO_2@TiO_2 architecture to address these limitations. This design not only enhances structural stability but also optimizes surface characteristics by providing a high-surface area framework for active site dispersion. The SiO_2 core acts as a thermal and mechanical stabilizer, while the TiO_2 shell ensures efficient light harvesting and charge generation. Building on this foundation, the incorporation of noble-metal-free bimetallic systems (eg., Cu/Fe, Ni/Co) introduces synergistic effects: one metal facilitates electron trapping, while the other promotes hole utilization, thereby minimizing recombination losses. This dual approach- combining structural control with strategic bimetallic doping- outperforms conventional single-dopant systems, as demonstrated in recent studies on cost-effective photocatalysts [50-52].

Table 2. Comparative study of previously reported reports on plasmonic effect on TiO_2 and SiO_2-based photocatalysts.

Sl no.	Photocatalyst	Light source	Target reaction	Reference
1	AgX-SiO_2 (X-Cl, Br, or I)	UV irradiation (320 nm to 400 nm) Visible light irradiation (420 nm)	Acetaldehyde (gas phase) Rhodamine B (5.4×10^{-5} M; liquid phase)	[53]
2	TiO_2-SiO_2-Ag	Visible light irradiation (420 nm) 150 W Xenon arc lamp with cutoff filter ($\lambda > 420$ nm)	96.9% Rhodamine B (10 ppm) degradation	[54]
3	SiO_2/TiO_2/20% $CuBiS_2$/2% Ag	Visible light irradiation with 150 W incandescent halogen lamp and UV irradiation with 450 W xenon light with cutoff filter ($\lambda > 420$ nm)	96% Acid black 1 (10 ppm) degradation	[55]
4	Ag/SiO_2/TiO_2	UV-visible-light irradiation: 300 W Xe lamp with water filter to cutoff IR	1.5×10^{-4} M aqueous salicylic acid (SA) and 1.5×10^{-4} M aniline (A)	[56]
5	M-TiO_2/SiO_2 (M: Pt^{4+}, Pd^{2+}, and Ag^{+})	300 W high pressure mercury (330 nm to 550 nm)	The pt-modified catalyst showed 2.8 time better photoactivity than the pristine catalyst. Brilliant red (K-2G) and cationic blue X-GRL (CBX)	[57]
6	TiO_2-SiO_2 (TS1) materials doped with Ag and Pt nanoparticles	Solar simulator box equipped with a Xe lamp (450 $W{\cdot}m^{-2}$) emitting the solar spectrum	TS1-Ag-1.0 and TS1-Pt-1.0 showed 2 and 5 times better photocatalytic phenol degradation than PS1	[58]
7	Au@SiO_2-TiO_2	UV irradiation (365 nm) Visible light irradiation (420 nm)	95% Methylene blue (2.4×10^{-5} M) degradation	[59]
8	SiO_2-Ag@TiO_2	Visible light irradiation, 350 W with UV cut filter ($\lambda > 420$ nm)	60% degradation of TC; 95.9% degradation of Rh-B. 10 $mg{\cdot}L^{-2}$ of TC 2×10^{-5} M of RhB, MB, and MV degradation	[60]
9	Core/shell nanostructures SiO_2/TiO_2 doped with Au nanoparticles	UV light ($I < 400$ nm)	Methyl orange (MO) degradation	[61]
10	Ag-coated SiO_2@TiO_2 (Ag-SiO_2@TiO_2) core-shell nanocomposites	500 W high-pressure mercury lamp	92.9% Phenol and 83.5% methylene blue degradation	[62]
11	Au-Loaded, N-TiO_2	10 $mW{\cdot}cm^{-2}$ fluroscent bulb	23.4 μmol H_2 evolution in 2 h	[63]
12	SiO_2@Ag NCs@Ag_3PO_4	150 W Xe lamp, cutoff filter 420 nm	2460 $\mu mol{\cdot}h^{-1}g^{-1}$ H_2 evolution	[14]
13	Cu-Ni SiO_2@TiO_2	150 W Xe lamp, cutoff filter 400 nm	89% phenol photooxidation 1560 $\mu mol{\cdot}h^{-1}g^{-1}$ H_2 evolution	[31]
14	Mn-TiO_2@SiO_2	150 W Xe lamp, cutoff filter 420 nm	reactive red 120, methyl orange, and methyl blue degradation	[64]
15	Co, Ni-bimetals incorporated SiO_2@TiO_2	Natural solar light (823 $W{\cdot}m^{-2}$)	88.4% Tetracycline degradation	Present study

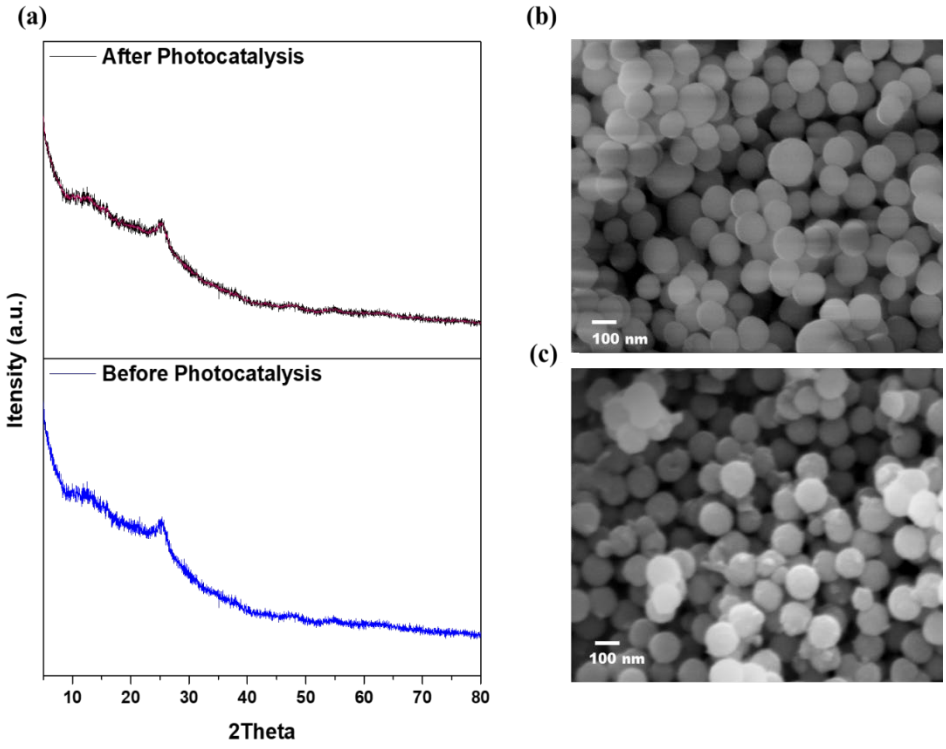

Figure 10. (a) XRD analysis before and after photocatalysis, (b) FE-SEM before photocatalysis, and (c) FE-SEM after photocatalysis using ST-Co, $Ni_{1:1}$ nanocomposite.

4. Conclusion

The successful fabrication of a bimetallic ST-Co, $Ni_{1:1}$ hybrid photocatalyst was achieved. A modified Stober technique was used to prepare spherical SiO_2 nanoparticles, which were then coated with an ultrathin layer of TiO_2 to form a core-shell structure. Then, a straightforward chemical reduction technique was used to deposit the Co-Ni alloy. The phase composition, crystal structure, optical characteristics, and photocatalytic efficacy were all carefully assessed. The ST-Co, $Ni_{1:1}$ was shown to have increased photocatalytic activity for tetracycline (TC) degradation. Plasmon-induced hot electron transfer from the Co-Ni alloy to the TiO_2 conduction band via a Schottky junction was the primary mechanism causing the photo-degradation. The maximum TC degradation rate achieved was 88.4% at an optimized pH of 5 and catalyst dosage of 0.04 g. Hydroxyl radicals ($^{\bullet}OH$) and holes (h^+) were identified as the primary reactive species, while superoxide ($^{\bullet}O_2^-$) and electrons (e^-) contributed to a lesser extent. The reaction follows pseudo-1st-order kinetics, and the catalyst demonstrated stability over four consecutive cycles. This study outlines an easy and cost-effective method for developing hybrid photocatalysts based on bimetallic alloys, offering a promising approach to reducing tetracycline pollution.

Acknowledgements

All the authors are thankful to the authority of Siksha 'O' Anusandhan, deemed to be a University in Odisha, India, CSIR-Institute of Materials and Minerals Technology, Bhubaneswar, Odisha, India for providing research facilities to carry out this work.

Author contribution

Pratyush Kumar Sahu: Conceptualization, Writing – original draft. Alaka Rath: Formal analysis. Aslisha Champati: Conceptualization, Abanti Pradhan: Formal Analysis. Ashish Madhual, Pravat Manjari Mishra: Characterization & Formal analysis. Brundabana Naik: Conceptualization, Supervision, Writing – review & editing.

Conflict of Interest

The authors declare that there is no competing interest in this manuscript.

References

[1] F. Saadati, N. Keramati, and M. M. Ghazi, "Influence of parameters on the photocatalytic degradation of tetracycline in wastewater: A review," *Critical Reviews in Environmental Science and Technology*, vol. 46, no. 8, pp. 757-782, 2016.

[2] J. W. Bennett and K.-T. Chung, "Alexander fleming and the discovery of penicillin," 2001.

[3] M. Ahmadi, H. R. Motlagh, N. Jaafarzadeh, A. Mostoufi, R. Saeedi, G. Baregar, and S. Jorfi, "Enhanced photocatalytic degradation of tetracycline and real pharmaceutical wastewater using MWCNT/TiO_2 nano-composite," *Journal of Environmental Management*, vol. 186, pp. 55-63, 2017.

[4] T. H. Grossman, "Tetracycline antibiotics and resistance," *Cold Spring Harb Perspect Medicine*, vol. 6, no. 4, p. a025387, 2016.

[5] S. Wu, H. Hu, Y. Lin, J. Zhang, and Y. H. Hu, "Visible light photocatalytic degradation of tetracycline over TiO_2," *Chemical Engineering Journal*, vol. 382, p. 122842, 2020.

[6] P. K. Sahu, A. Champati, A. Pradhan, N. K. Sahoo, and B. Naik, "Monoclinic ZrO_2 nanospheres supported nitrogen-enriched carbon nitride nanosheets for efficient photodegradation of ciprofloxacin," *Journal of Nanoparticle Research*, vol. 26, no. 11, p. 261, 2024.

[7] L.-A. P. Thi, S. C. Panchangam, H.-T. Do, and V.-H. Nguyen, "Prospects and challenges of photocatalysis for degradation and mineralization of antiviral drugs," *Nanostructured Photocatalysts*, pp. 489-517, 2021.

[8] S. Nagarajan, N. C. Skillen, F. Fina, G. Zhang, C. Randorn, L. A. Lawton, J. T. S. Irvine, and P. K. J. Robertson, "Comparative assessment of visible light and UV active photocatalysts by hydroxyl radical quantification," *Journal of Photochemistry and Photobiology A: Chemistry*, vol. 334, pp. 13-19, 2017.

[9] J. Liu, G. Dong, J. Jing, S. Zhang, Y. Huang, and W. Ho, "Photocatalytic reactive oxygen species generation activity of TiO_2 improved by the modification of persistent free radicals," *Environmental Science: Nano*, vol. 8, no. 12, pp. 3846-3854, 2021.

[10] J. W. Leem, S.-R. Kim, K.-H. Choi, and Y. L. Kim, "Plasmonic photocatalyst-like fluorescent proteins for generating reactive oxygen species," *Nano Convergence*, vol. 5, pp. 1-14, 2018.

[11] X. Li, G. Fang, T. Wu, Q. Tian, Q. Yang, and Z. Chen, "Sunlight-driven superoxide radicals generation from double-modified carbon nitride for efficient lignin β-O-4 bonds photocleavage," *Applied Surface Science*, vol. 635, p. 157717, 2023.

[12] J. Wen, J. Xie, X. Chen, and X. Li, "A review on g-C_3N_4-based photocatalysts," *Applied Surface Science*, vol. 391, pp. 72-123, 2017.

[13] A. Subhadarshini, E. Subudhi, P. G. R. Achary, S. A. Behera, N. Parwin, and B. Nanda, "ZIF-8 supported Ag_3PO_4/g-C_3N_4 a Double Z-scheme heterojunction: An efficient photocatalytic, antibacterial and hemolytic nanomaterial," *Journal of Water Process Engineering*, vol. 65, p. 105901, 2024.

[14] S. Mohanty, P. Babu, K. Parida, and B. Naik, "Surface-plasmon-resonance-induced photocatalysis by core-shell SiO_2@Ag NCs@Ag_3PO_4 toward water-splitting and phenol oxidation reactions," *Inorganic Chemistry*, vol. 58, no. 15, pp. 9643-9654, 2019.

[15] J. Zhang, G. Yu, C. Yang, and S. Li, "Recent progress on S-scheme heterojunction strategy enabling polymer carbon nitrides C3N4 and C3N5 enhanced photocatalysis in energy conversion and environmental remediation," *Current Opinion in Chemical Engineering*, vol. 45, p. 101040, 2024.

[16] C. Liu, J. Zhang, W. Wang, L. Chen, and M. Zhu, "Progress in the synthesis and applications of N-rich carbon nitride (C_3N_5)-based catalysts in environmental and energy catalysis," *Surfaces and Interfaces*, vol. 42, p. 103491, 2023.

[17] A. K. Ganguli, A. Das, and K. Natarajan, "Core-shell type semiconducting heterostructures for visible light photocatalysis," *Chemical Record*, vol. 20, no. 5, pp. 371-388, 2020.

[18] M. Maniyazagan, P. Naveenkumar, H.-W. Yang, H. Zuhaib, W. S. Kang, and S.-J. Kim, "Hierarchical SiO_2@ $FeCo_2O_4$ core--shell nanoparticles for catalytic reduction of 4-nitrophenol and degradation of methylene blue," *Journal of Molecular Liquids*, vol. 365, p. 120123, 2022.

[19] P. Babu, H. Park, and J. Y. Park, "Surface chemistry of graphitic carbon nitride: doping and plasmonic effect, and photocatalytic applications," *Surface Science and Technology*, vol. 1, no. 1, p. 29, 2023.

[20] N. Hikmah, N. F. Idrus, J. Jai, and A. Hadi, "Synthesis and characterization of silver-copper core-shell nanoparticles using polyol method for antimicrobial agent," in *IOP conference series: Earth and environmental science*, 2016, p. 12050.

[21] P. K. Sahu, A. Champati, A. Pradhan, and B. Naik, "Design and development of nanostructured photocatalysts for large-scale solar green hydrogen generation," *Sustainable Energy & Fuels*, vol. 8, no. 9, pp. 1872-1917, 2024.

[22] H.-Y. Zhu, M.-T. Liu, G. Wang, R.-R. Du, H.-Y. Zhao, H. Lu, S.-Q. Yang, S. Tang, Z.-J. Guo, J. Yang, C.-Z. Zhu, and F. Yang, "Constructing core@ shell structured photothermal nanosphere with thin carbon layer confined Co-Mn bimetals for pollutant degradation and solar interfacial water evaporation," *Rare Metals*, vol. 43, no. 4, pp. 1686-1701, 2024.

[23] H. Lai, W. Xiao, S. Yi-Wang, T. Song, B. Long, S. Yin, A. Ali, and G.-J. Deng, "Plasmon-induced carrier separation boosts high-selective photocatalytic CO_2 reduction on dagger-axe-like Cu@ Co core--shell bimetal," *Chemical Engineering Journal*, vol. 417, no. 18, p. 129295, 2021.

[24] C.-W. Kang, and H. Kolya, "Green synthesis of Ag-Au bimetallic nanocomposites using waste tea leaves extract for degradation congo red and 4-Nitrophenol," *Sustainability*, vol. 13, no. 6, p. 3318, 2021.

[25] S. Mishra, N. Chakinala, A. G. Chakinala, and P. K. Surolia, "Photocatalytic degradation of methylene blue using monometallic and bimetallic Bi-Fe doped TiO_2," *Catalysis Communications*, vol. 171, p. 106518, 2022.

[26] N. Talreja, S. Afreen, M. Ashfaq, D. Chauhan, A. C. Mera, C. A. Rodriguez, and R. V. Mangalaraja, "Bimetal (Fe/Zn) doped BiOI photocatalyst: An effective photodegradation of tetracycline and bacteria," *Chemosphere*, vol. 280, p. 130803, 2021.

[27] S. Li, C. You, K. Rong, C. Zhuang, X. Chen, and B. Zhang, "Chemically bonded Mn0. 5Cd0. 5S/BiOBr S-scheme photo-catalyst with rich oxygen vacancies for improved photocatalytic decontamination performance," *Advanced Powder Materials*, vol. 3, no. 3, p. 100183, 2024.

[28] C. Shen, X. Li, B. Xue, D. Feng, Y. Liu, F. Yang, M. Zhang, and S. Li, "Surface plasmon effect combined with S-scheme charge migration in flower-like Ag/$Ag_6Si_2O_7$/$Bi_{12}O_{17}Cl_2$ enables efficient photocatalytic antibiotic degradation," *Applied Surface Science*, vol. 679, p. 161303, 2025.

[29] S. Li, C. You, Q. Xue, Y. Zhao, F. Yang, Y. Liu, L. Bai, M. Zhang, and C. Zhuang, "Carbon quantum dots and interfacial chemical bond synergistically modulated S-scheme $Mn_{0.5}Cd_{0.5}S$/BiOBr photocatalyst for efficient water purification," *Journal of Materials Science & Technology*, vol. 214, pp. 255-265, 2025.

[30] Preeti, S. Mishra, N. Chakinala, A. G. Chakinala, and P. K. Surolia, "Bimetallic Bi/Zn decorated hydrothermally synthesized

TiO_2 for efficient photocatalytic degradation of nitrobenzene," *Catalysis Communications.*, vol. 172, p. 106538, 2022.

[31] P. Babu, and B. Naik, "Cu--Ag bimetal alloy decorated SiO_2 @TiO_2 hybrid photocatalyst for enhanced H_2 evolution and phenol oxidation under visible light," *Inorganic Chemistry.*, vol. 59, no. 15, pp. 10824-10834, 2020.

[32] P. Babu, S. R. Dash, and K. Parida, "Mechanistic insight the visible light driven hydrogen generation by plasmonic Au-Cu alloy mounted on TiO_2@ B-doped g-C_3N_4 heterojunction photocatalyst," *Journal of Alloys and Compounds*, vol. 909, p. 164754, 2022.

[33] S. Ikeda, H. Kobayashi, Y. Ikoma, T. Harada, T. Torimoto, B. Ohtani, and M. Matsumura, "Size-selective photocatalytic reactions by titanium (IV) oxide coated with a hollow silica shell in aqueous solutions," *Physical Chemistry Chemical Physics*, vol. 9, no. 48, pp. 6319-6326, 2007.

[34] Y. Ren, M. Chen, Y. Zhang, and L. Wu, "Fabrication of rattle-type TiO_2/SiO_2 core/shell particles with both high photo-activity and UV-shielding property," *Langmuir*, vol. 26, no. 13, pp. 11391-11396, 2010.

[35] D. Burak, J. H. Han, J. S. Han, I. S. Kim, M. A. Rahman, J. K. W. Yang, and S.-H. Cho, "Controlling TiO_2 photocatalytic behaviour via perhydropolysilazane-derived SiO_2 ultrathin shell," *Nanoscale*, vol. 16, no. 47, pp. 21960-21969, 2024.

[36] B. K. Mutuma, X. Mathebula, I. Nongwe, B. P. Mtolo, B. J. Matsoso, R. Erasmus, Z. Tetana, and N. J. Coville, "Unravelling the interfacial interaction in mesoporous SiO_2@nickel phyllosilicate/TiO_2 core--shell nanostructures for photocatalytic activity," *Beilstein Journal of Nanotechnology*, vol. 11, no. 1, pp. 1834-1846, 2020.

[37] B. R. Gomes, J. L. Lopes, L. Coelho, M. Ligonzo, M. Rigoletto, G. Magnacca, and F. Deganello, "Development and upscaling of SiO_2@TiO_2 core-shell nanoparticles for methylene blue removal," *Nanomaterials*, vol. 13, no. 16, p. 2276, 2023.

[38] M. Dolatyari, M. Tahmasebi, S. Dolatyari, A. Rostami, A. Zarghami, A. Yadav, and A. Klein, "Core/Shell ZnO/TiO_2, SiO_2/TiO_2, Al_2O_3/TiO_2, and $Al_{1.9}Co_{0.1}O_3$/TiO_2 Nanoparticles for the Photodecomposition of Brilliant Blue E-4BA," *Inorganics*, vol. 12, no. 11, p. 281, 2024.

[39] N. Jumrus, N. Thepthip, R. Siriariyachai, A. Panthawan, W. Sroila, E. Kantarak, N. Jhuntama, W. Thongpan, T. Kumpika, P. Singjai, and W. Thongsuwan, "Optimizing drying time of lacquer-based MTCS-modified SiO_2-TiO_2 coatings for enhanced mechanical durability, superhydrophobicity and photocatalytic activity," *Applied Surface Science*, vol. 680, p. 161444, 2025.

[40] R. P. Galhenage, H. Yan, S. A. Tenney, N. Park, G. Henkelman, P. Albrechi, D. Mullins, and D. Chen, "Understanding the nucleation and growth of metals on TiO_2: Co compared to Au, Ni, and Pt," *The Journal of Physical Chemistry C*, vol. 117, no. 14, pp. 7191-7201, 2013.

[41] A. Fujishima, X. Zhang, and D. A. Tryk, "TiO_2 photocatalysis and related surface phenomena," *Surface Science Reports*, vol. 63, no. 12, pp. 515-582, 2008.

[42] T. S. Lilge, A. R. N. Stigger, C. D. Fernandes, L. T. Gularte, C. W. Raubach, S. da S. Cava, P. L. G. Jardim, M. E. G. Valerio, and M. L. Moreira, "Increase of Voc using heterojunctions of $BaTiO_3$ without sensitization," *Ceramics International*, vol. 46, no. 4, pp. 4907-4913, 2020.

[43] X. Chen, and S. S. Mao, "Titanium dioxide nanomaterials: synthesis, properties, modifications, and applications," *Chemical Reviews*, vol. 107, no. 7, pp. 2891-2959, 2007.

[44] M. Kosmulski, "The pH dependent surface charging and points of zero charge. X. Update," *Advances in Colloid and Interface Science*, vol. 319, p. 102973, 2023.

[45] D. O. Antonov, D. P. Tambasova, A. B. Shishmakov, I. A. Kirilyuk, and E. G. Kovaleva, "Acidic and electrosurface properties of binary TiO_2-SiO_2 xerogels using EPR of pH-sensitive nitroxides," *Gels*, vol. 7, no. 3, p. 119, 2021.

[46] M. Kosmulski, "The pH dependent surface charging and points of zero charge. IX. update," *Advances in Colloid and Interface Science*, vol. 296, p. 102519, 2021.

[47] P. Pu, H. Cachet, N. Laidani, and E. M. M. Sutter, "Influence of pH on surface states behavior in TiO2 nanotubes," *Journal of Physical Chemistry C*, vol. 116, no. 42, pp. 22139-22148, 2012.

[48] L. Wang, G. Xie, X. Mi, B. Zhang, Y. Du, Q. Zhu, and Z. Yu, "Surface-modified TiO_2@SiO_2 nanocomposites for enhanced dispersibility and optical performance to apply in the printing process as a pigment," *ACS omega*, vol. 8, no. 22, pp. 20116-20124, 2023.

[49] M. Zhang, M. Liu, Y. Jiang, J. Li, and Q. Chen, "Synthesis of immobilized CdS/TiO_2 nanofiber heterostructure photocatalyst for efficient degradation of toluene," *Water, Air, & Soil Pollution*, vol. 231, pp. 1-11, 2020.

[50] W.-L. Li, Q. Tang, L.-L. Gao, Y.-Q. Shen, B. Yu, and H.-L. Cong, "Preparation of multilayered core-shell TiO_2@ DR@ SiO_2 composites and investigation of its photocatalytic performance," *Integrated Ferroelectrics*, vol. 190, no. 1, pp. 142-148, 2018.

[51] H. Lu, J. Tournet, K. Dastafkan, Y. Liu, Y. H. Ng, S. K. Karuturi, C. Zhao, and Z. Yin, "Noble-metal-free multicomponent nano-integration for sustainable energy conversion," *Chemical Reviews*, vol. 121, no. 17, pp. 10271-10366, 2021.

[52] J. Schneider, M. Matsuoka, M. Takeuchi, J. Zhang, Y. Horiuchi, M. Anpo, and D. W. Bahnemann, "Understanding TiO_2 photo-catalysis: mechanisms and materials," *Chemical Reviews,* vol. 114, no. 19, pp. 9919-9986, 2014.

[53] D. B. Hamal, and K. J. Klabunde, "Heterogeneous photocatalysis over high-surface-area silica-supported silver halide photocatalysts for environmental remediation," in *Nanoscale materials in chemistry: Environmental applications*, ACS Publications, 2010, pp. 191-205.

[54] C. Liu, D. Yang, Y. Jiao, Y. Tian, Y. Wang, and Z. Jiang, "Biomimetic synthesis of TiO_2--SiO_2--Ag nanocomposites with enhanced visible-light photocatalytic activity," *ACS Applied Materials & Interfaces*, vol. 5, no. 9, pp. 3824-3832, 2013.

[55] H. Abdullah, and D.-H. Kuo, "Photocatalytic performance of Ag and $CuBiS_2$ nanoparticle-coated SiO_2@TiO_2 composite sphere under visible and ultraviolet light irradiation for azo dye degradation with the assistance of numerous nano p--n diodes," *Journal of Physical Chemistry C*, vol. 119, no. 24, pp. 13632-13641, 2015.

[56] J. E. Lee, S. Bera, Y. S. Choi, and W. I. Lee, "Size-dependent plasmonic effects of M and M@SiO_2 (M= Au or Ag) deposited on TiO_2 in photocatalytic oxidation reactions," *Applied Catalysis B: Environmental*, vol. 214, pp. 15-22, 2017.

[57] C. Hu, Y. Tang, Z. Jiang, Z. Hao, H. Tang, and P. K. Wong, "Characterization and photocatalytic activity of noble-metal-supported surface TiO_2/SiO_2," *Applied Catalysis A: General*, vol. 253, no. 2, pp. 389-396, 2003.

[58] J. Matos, B. Llano, R. Montaña, P. S. Poon, and M. C. Hidalgo, "Design of Ag/and Pt/TiO_2-SiO_2 nanomaterials for the photocatalytic degradation of phenol under solar irradiation," *Environmental Science and Pollution Research* vol. 25, pp. 18894-18913, 2018.

[59] J.-J. Chen, J. C. S. Wu, P. C. Wu, and D. P. Tsai, "Improved photocatalytic activity of shell-isolated plasmonic photocatalyst Au@SiO_2/TiO_2 by promoted LSPR," *Journal of Physical Chemistry C*, vol. 116, no. 50, pp. 26535-26542, 2012.

[60] Y. Zhang, J. Chen, H. Tang, Y. Xiao, S. Qiu, S. Li, and S. Cao, "Hierarchically-structured SiO_2-Ag@TiO_2 hollow spheres with excellent photocatalytic activity and recyclability," *Journal of Hazardous Materials*, vol. 354, pp. 17-26, 2018.

[61] R. Lee, Y. Kumaresan, S. Y. Yoon, S. H. Um, I. K. Kwon, and G. Y. Jung, "Design of gold nanoparticles-decorated SiO_2 @TiO_2 core/shell nanostructures for visible light-activated photocatalysis," *RSC Advances,* vol. 7, no. 13, pp. 7469-7475, 2017.

[62] N. Fu, X. Ren, and J. Wan, "Preparation of Ag-coated SiO_2@ TiO_2 core-shell nanocomposites and their photocatalytic applications towards phenol and methylene blue degradation," *Journal of Nanomaterials.*, vol. 2019, no. 1, p. 8175803, 2019.

[63] B. Naik, S. M. Kim, C. H. Jung, S. Y. Moon, S. H. Kim, and J. Y. Park, "Enhanced H_2 generation of Au-loaded, nitrogen-doped TiO_2 hierarchical nanostructures under visible light," *Advanced Materials Interfaces* vol. 1, no. 1, p. 1300018, 2014.

[64] X. Tian, X. Cai, Z. Zeng, Y. He, X. Xu, L. Lei, C. Xu, X. Xu, Y. Xu, P. Li, and X. Zhang, "Mn doping and core-shell engineering of silane-modified Mn-TiO_2@SiO_2 nanoparticles with drastically reduced photocatalytic activity for transparent UV-shielding hybrid materials," *Chemical Engineering Journal*, vol. 498, p. 155304, 2024.